

Ultralow $1/f$ Noise in a Heterostructure of Superconducting Epitaxial Cobalt-Disilicide Thin Film on Silicon

Shao-Pin Chiu,[†] Sheng-Shiuan Yeh,[†] Chien-Jyun Chiou,[‡] Yi-Chia Chou,^{,‡} Juhn-Jong Lin,^{*,†,‡}
and Chang-Chyi Tsuei[§]*

[†]Institute of Physics, National Chiao Tung University, Hsinchu 300, Taiwan

[‡]Department of Electrophysics, National Chiao Tung University, Hsinchu 300, Taiwan

[§]IBM Thomas J. Watson Research Center Yorktown Heights, NY 10598, U.S.A.

KEYWORDS: Superconducting silicide/silicon heterostructure, interfacial dynamic defects, $1/f$ resistance noise, dimer reconstruction, two-level-system fluctuators

ABSTRACT: High-precision resistance noise measurements indicate that the epitaxial CoSi_2/Si heterostructures at 150 K and 2 K (slightly above its superconducting transition temperature T_c of 1.54 K) exhibit an unusually low $1/f$ noise level in the frequency range of 0.008–0.2 Hz. This corresponds to an upper limit of Hooge constant $\gamma \leq 3 \times 10^{-6}$, about 100 times lower than that of single-crystalline aluminum films on SiO_2 capped Si substrates. Supported by high-resolution cross-sectional transmission electron microscopy studies, our analysis reveals that the $1/f$ noise is

dominated by excess interfacial Si atoms and their dimer reconstruction induced fluctuators. Unbonded orbitals (*i.e.*, dangling bonds) on excess Si atoms are intrinsically rare at the epitaxial CoSi₂/Si(100) interface, giving limited trapping-detrapping centers for localized charges. With its excellent normal-state properties, CoSi₂ has been used in silicon-based integrated circuits for decades. The intrinsically low noise properties discovered in this work could be utilized for developing quiet qubits and scalable superconducting circuits for future quantum computing.

Superconducting circuit-based qubits technology represents the best hope of building a scalable fault-tolerant quantum computer.¹⁻³ The qubit coherence time has been increased dramatically from about 1 ns to 100 μs during the last decade.^{3,4} Since quantum states are intrinsically fragile, errors are bound to occur in the course of any quantum computing process. Quantum error correction (QEC) is essential for quantum computation. However, even with the presently available superconducting qubits, tremendous complexity in developing a viable and feasible QEC architecture is unavoidable.^{3,4} Even when the recently proposed surface code QEC approach is employed, one needs 10³ to 10⁴ physical qubits to define and operate one logical qubit.⁵ This would involve a significant amount of extra interactions with the environment and represent sources of decoherence. To solve this daunting problem one must improve the coherence time at least by another factor of ten. To achieve this goal, except focusing on the improvement of clever qubit design and cryogenic microwave engineering, an alternative, valuable strategy is to find a practicable superconducting material which is essentially free of decoherence sources. In other words, it is desirable to fabricate and demonstrate a superconducting heterostructure with material properties superior to the commonly used Al/AlO_x-based heterostructures.

The coupling of a superconducting device with its environmental degrees of freedom results in detrimental fluctuations (noises) of charge, critical current or flux which, in turn, deteriorate the

ultimate performance of the device. Recently, a variety of noise sources in superconducting quantum interference devices (SQUIDs) and qubits have been identified.^{6,7} By and large, these decoherence sources manifest low-frequency noise in the form of a $1/f$ power spectrum density (PSD). Microscopically, they are believed to be closely associated with the defects residing at the superconductor/insulator interfaces and within the dielectric barrier.⁷⁻⁹ Thus, an ideal candidate of such heterostructure should possess high-quality epitaxial interface with essentially no fluctuating atomic structures and charge trap centers. If charge transport in the epitaxial superconducting layer (in the normal state) is mainly limited by the boundary scattering at the superconductor/insulator interface,¹⁰ the resistance noise measurements on such a heterostructure at $T > T_c$ can be used to characterize the dynamic properties of the interfacial structural defects as well as the low-frequency noise in superconducting devices such as qubits and SQUIDs.

The cobalt disilicide (CoSi_2), a compound with a sharp superconducting transition at $T_c \approx 1.5 \text{ K}$,¹¹ is known for its excellent epitaxial properties on silicon,¹² single crystallinity with long carrier elastic mean free path,¹⁰ robust covalent bond,¹³ and relatively strong spin-orbit coupling.¹⁴ Due to its good thermal stability and low resistivity ($\rho(300 \text{ K}) \approx 15 \mu\Omega \text{ cm}$), it was widely used as interconnects and metallic contacts in CMOS and other electronic devices for years.¹⁵ In this work, we show that this superconductor-silicon heterostructure possesses ultralow $1/f$ resistance noise at $T \geq 2 \text{ K}$, and hence has high potential for applications in superconducting-circuit based quantum computing as well as other superconductive devices.

Since the 1970s the transition-metal disilicides, such as CoSi_2 and NiSi_2 , have been widely used in the semiconductor (Si) circuit devices. Various synthesis methods and fabrication conditions were shown to sensitively influence the growth kinetics and microstructures of the disilicides formed on silicon.^{12,15,16} Since CoSi_2 has a very small lattice mismatch with Si (-1.2%) and it is

the only congruently melted intermetallic compound in the Co-Si alloy system, an epitaxial single-crystalline phase of CoSi_2 can be readily fabricated on a (100) or (111) Si substrate. In this study, we employ the standard deposition and thermal annealing technique to grow an epitaxial CoSi_2 film at the Co/Si(100) interface. We note that using the Si(100) substrates has twofold advantages. First, it is fully compatible with the present-day semiconductor integrated-circuit technology. Second, it leads to a dangling-bond-free CoSi_2 top surface,^{17,18} and hence diminishing the $1/f$ noise sources in the CoSi_2/Si heterostructure. Consequently, the remaining possible noise sources are the defects at the epitaxial $\text{CoSi}_2/\text{Si}(100)$ interface. This is the focus of the present work.

RESULTS AND DISCUSSION

Figure 1(a) shows the grazing x-ray diffraction (GIXRD) spectra for our samples, as indicated. The preferred orientations of (111), (220) and (311), manifesting good crystallinity, are clearly seen in epitaxial films. This result suggests that the CoSi_2 phase already formed with 30 min annealing at 800 °C. For comparison, Figure 1(a) also shows that such peaks are barely seen in a non-epitaxial CoSi_2 film nor a pure Co film. Transmission electron microscopy (TEM) studies indicate that the as-grown epitaxial CoSi_2 phase is single-crystalline along the direction normal to the film surface, while with a large grain size of ~ 300 nm in the lateral direction.¹⁹ Figure 1(b) shows the variation of resistivity with temperature for the 30, 60 and 90 min annealed epitaxial CoSi_2 films, as indicated. The inset shows that the overall temperature dependences are similar, manifesting that of a good metal. The residual resistivities $\rho(2\text{ K}) \approx 2.5 - 3 \mu\Omega\text{ cm}$ are low, while the T_c is compatible to that of Al. In particular, a sharp superconducting transition occurs at 1.54 K in the 90 min annealed film. Such a high T_c value can only be realized in CoSi_2 with the highest possible crystal quality.²⁰ In contrast, a two-step transition, accompanied with a transition tail, is found in the 30 (60) min annealed film, indicating that the sample structure is slightly

inhomogeneous. Combining the resistivity results with high-resolution TEM studies (Figure 2), we can explain the two-step transition in terms of the presence of a Moiré fringe regime whose T_c value is slightly reduced from 1.54 K. Figure 1(c) shows the superconducting transitions for a non-epitaxial and a 90 min annealed epitaxial CoSi₂ films, as indicated. A reduced T_c value, accompanied by a broad two-step transition is evident in the non-epitaxial film, indicating significant inhomogeneous lattice structure.

Figure 1(d) shows the magnetoresistance (MR) for an epitaxial CoSi₂ film at 10 K. The magnetic field was applied perpendicular to the film plane. A positive, quadratic MR (see inset) was observed, suggesting a classical MR due to the Lorentz force and a long elastic mean free time/path of the charge carriers in the sample.^{10,14} That is, the normalized MR is given by $[R(B) - R(0)]/R(0) \approx (\mu B)^2$, where $\mu = e\tau_e/m^*$ is the mobility, e is the electronic charge, τ_e is the elastic mean free time, and m^* is the effective carrier mass. In CoSi₂, $m^* \approx m_0$, the free electron mass.¹⁴ The carrier (hole) concentration n in CoSi₂ epitaxial films on Si(100) has been measured *via* Hall effect to be $n \approx 2.5 \times 10^{22} \text{ cm}^{-3}$,^{14,21} giving rise to a Fermi energy of $E_F \approx 3.1 \text{ eV}$ and a Fermi velocity of $v_F \approx 1.05 \times 10^6 \text{ m/s}$ through the free-electron model. We then evaluated the elastic mean free path to be $l_e = v_F \tau_e \approx 120 \text{ nm}$ in the 90 min annealed epitaxial CoSi₂. From the film thickness dependence on residual resistivities and MRs (Supporting Information S1), we found a bulk value of the elastic mean free path being $l_e \approx 363 \text{ nm}$ in epitaxial CoSi₂/Si(100). Thus, surface/interface scattering plays a significant role in our 105 nm thick CoSi₂ films. On the other hand, we obtain a relatively short mean path of $l_e \approx 10 \text{ nm}$ in the non-epitaxial films. Table 1 lists the relevant parameters for various CoSi₂ films studied in this work.

Table 1. Relevant parameters for three epitaxial and one non-epitaxial CoSi₂ films.*

| Sample | ρ (290 K) ($\mu\Omega$ cm) | ρ (10 K) ($\mu\Omega$ cm) | T_c (K) | ΔT_c (K) | l_e (nm) | t_M (nm) |
|-----------------|-------------------------------------|------------------------------------|-----------|------------------|------------|---------------|
| 30 min annealed | 16.3 | 2.98 | 1.53 | 0.013 | 101 | 23 |
| 60 min annealed | 15.0 | 2.5 | 1.53 | 0.014 | 119 | 12 |
| 90 min annealed | 15.0 | 2.5 | 1.54 | 0.005 | 121 | 0 |
| non-epitaxial | 44 | 27.2 | 0.98 | 0.145 | 10 | – |

* T_c is defined as the temperature corresponding to 50% of the normal-state resistance (R_N). The transition width ΔT_c is defined as the temperature difference between the T values corresponding to 10% and 90% of R_N . t_M is the thickness of Moiré fringe region.

Figures 2(a)–(d) show the high-resolution cross-sectional transmission electron microscopy (XTEM) images of the CoSi₂/Si interface for the 30, 60, 90 and 90 min annealed films, respectively. It is clear that the CoSi₂ phase is epitaxial with the Si(100) substrate. On the CoSi₂ side, Moiré fringes are seen in the 30 and 60 min annealed films, but absent in the 90 min annealed films. The stripes in the right insets of Figures 2(a) and 2(b) show that the Moiré fringes extend for ≈ 23 and ≈ 12 nm from the interface in the 30 and 60 min annealed films, respectively. We ascribe the formation of the Moiré fringes to the lattice misfits and misorientations,²² which induced strains near the CoSi₂/Si interface. In Figure 3, we present atomic simulations to illustrate that the Moiré fringes can be generated by rotating several CoSi₂ atomic layers against the bulk. In addition, in both 30 and 60 min annealed films, extra spots due to superlattice layers are seen in the diffraction patterns on the CoSi₂ side, see the left insets of Figures. 2(a) and 2(b), implying that the silicidation process was incomplete near the interface. With 90 min annealing, the phase transformation from Si to CoSi₂ was complete, and the strains were released by the formation of dislocations at the interface, rendering an atomically sharp interface without Moiré fringes, Figures. 2(c) and 2(d).

From the diffraction patterns shown in the insets of Figures 2(a)–(c), we found the expected epitaxy of $\text{CoSi}_2(100)$ on $\text{Si}(100)$ for all three annealing time periods, corresponding to the epitaxial relation $\text{CoSi}_2[011] // \text{Si}[011]$ and $\text{CoSi}_2(200) // \text{Si}(200)$. In Figure 2(d), another epitaxy of $\text{CoSi}_2(110)$ on $\text{Si}(100)$ was found, corresponding to the epitaxial relation $\text{CoSi}_2[011] // \text{Si}[011]$ and $\text{CoSi}_2(022) // \text{Si}(111)$.^{12,15,22} The right inset of Figure 2(d) shows a zoom-in image for the latter epitaxial relation, highlighted with blue (Co) and yellow (Si) balls. These two kinds of epitaxial relation often compete in the $\text{CoSi}_2/\text{Si}(100)$ system. Judging from our fabrication conditions and the measured GIXRD results, we expect a small regime of our film possess the epitaxy of $\text{CoSi}_2(100)$ on $\text{Si}(100)$,^{12,15,22} while the rest possess the epitaxy of $\text{CoSi}_2(110)$ on $\text{Si}(100)$. In the regime with the epitaxy of $\text{CoSi}_2(100)$ on $\text{Si}(100)$, a candidate unstable interfacial structure, the 2×1 dimer reconstruction, is known to exist,²³⁻²⁷ which arises from the dimerization of excess Si at the interface.²³ Indeed, we found dimer reconstructions in the 90 min annealed sample, see the high magnification XTEM images in Figure 5(a) and further discussion below.

In the 30 min annealed film, pronounced Moiré fringes exist on the CoSi_2 side as indicated in the XTEM image of Figure 2(a). We replot Figure 2(a) into Figure 3(a) and show corresponding atomic simulations in Figure 3(b). The simulated fringes in Figure 3(b) reveal oblique stripes which were generated by a 50° rotational shift between two sets of $\text{CoSi}_2(011)$ planes with respect to the $[011]$ axis. Furthermore, if structural defects such as edge dislocations are present in the CoSi_2 lattice, the generated Moiré fringes will contain distortions. This is indeed the case occurs in the dashed oval region in Figure 3(a). Corresponding atomic simulations are illustrated in the inset of Figure 3(b). In addition, atomic misfits at the CoSi_2/Si interface can possibly cause kinked or stepwise boundaries, such as those indicated by the blue arrow in Figure 3(a) and correspondingly by the red arrows in Figure 3(b). From our electrical-transport studies and the

parameters listed in Table 1 for the three epitaxial films, we clearly see that the presence of more pronounced Moiré fringes gives rise to higher residual resistivities, shorter elastic mean free paths, and wider superconducting transition widths.

The imperfection scattering centers in a metallic film can be categorized into two groups: static defects and dynamic defects (or dynamical structural defects). In the high-quality epitaxial CoSi₂/Si system, we expect that both types of defects are rare and reside mainly at the interface. Therefore, the charge transport properties are essentially governed by the boundary scattering, because, as aforementioned, the carrier elastic mean free path extracted from MRs is mainly limited by the film thickness. With this property the microscopic properties of interfacial dynamic defects can be detected through the measurement of resistance fluctuations.

We have carried out resistance noise studies of epitaxial CoSi₂ films using a high-resolution ac bridge technique schematically shown in Figure 4(a) (also see Methods). The dynamical structural defects can be modeled as two-level systems (TLSs) which induce fluctuations of scattering cross sections owing to their repeated relaxation processes.^{28,29} It is well known that if the distribution of the TLS activation energy is broad and flat, the voltage noise power spectrum density (PSD), S_V , for an ohmic conductor carrying a constant current would show $1/f$ dependence. This is widely described by the empirical Hooge expression^{28,29}

$$S_V = \gamma \frac{V^2}{N_c f} + S_V^0 \quad (1)$$

where the first term is the voltage noise PSD of the sample, and the second term is the background noise including the Johnson-Nyquist noise and the electronic noise from the measurement circuit. γ is the dimensionless Hooge parameter, V is twice of the root-mean-square voltage drop $\langle V_1 \rangle$

across one half of the sample (Figure 4(a)), and N_c is the total number of charge carriers in the sample.

In the following discussion, we focus on three types of 90 min annealed samples: sample type A (C) is an epitaxial CoSi_2 film without (with) dilute HF treatment of the CoSi_2 top surface before depositing Ti/Au electrodes, and sample type B is a non-epitaxial CoSi_2 film with dilute HF treatment. The dilute HF treatment was aimed at removing the thin native oxide layer on the CoSi_2 surface in order to ensure a good electrical contact between CoSi_2 and Ti/Au. The measured voltage noise PSDs of samples type A and type C at 150 K are shown in Figures. 4(b) and 4(d), respectively. The background PSD (black curves) $S_V(V_1 = 0) \approx 6 \times 10^{-18} \text{ V}^2/\text{Hz}$ indicates the resolution limit of our setup, which is just the input noise level of the preamplifier. In Figures. 4(b) and 4(d), the PSDs at finite bias voltages reveal $1/f$ dependence in the frequency range of $\sim 0.06 - 2 \text{ Hz}$ and $\sim 0.008 - 0.2 \text{ Hz}$, respectively. For both types of samples, we plot the variation of $\langle fS_V \rangle$ with V^2 in Figures. 4(c) and 4(e). Linear dependence of $\langle fS_V \rangle$ on V^2 is evident, as expected from the prediction of Eq. (1). However, it should be emphasized that the fitted slopes, *i.e.*, the γ/N_c values, for samples type A and type C are distinctly different. We obtain $\gamma \approx (1.4 \pm 0.2) \times 10^{-2}$ for sample type A, as compared to the extremely small value of $\gamma \approx (2.8 \pm 0.3) \times 10^{-6}$ for sample type C.

In summary, Figure 4(f) shows the normalized voltage noise PSD, $N_c S_V / V^2$, for three types of samples measured at 150 K, as indicated. Also included are representative data for a polycrystalline Al film at 300 K (taken from ref. 32) as well as a single-crystalline Al film at 150 K (taken from ref. 33). In all cases, the f^{-1} frequency dependence (dashed and dotted lines) is evident. The measured noise levels of these samples differ significantly and are sensitive to sample

preparation conditions. The larger PSD signal found in sample type A resulted from the large contact noise due to the highly resistive native oxide layer. The extracted γ value is $\sim 10^{-3} - 10^{-2}$. For sample type B, a non-epitaxial CoSi_2 film with dilute HF treatment, a notable decrease by ~ 2 orders of magnitude in the noise PSD was found ($\gamma \sim 1 \times 10^{-4}$). For sample type C with dilute HF treatment, the measured noise PSD is even lowered by another two orders of magnitude ($\gamma \approx 3 \times 10^{-6}$). Such an extremely low level of noise definitely deserves attention. First, we point out that our sample resistance is small ($R < 100 \Omega$), rendering a very low thermal noise PSD ($S_{V_thermal} = 4k_B TR \leq 8.3 \times 10^{-19} \text{ V}^2/\text{Hz}$ at 150 K, where k_B is the Boltzmann constant). Thus, the flattening in the PSD of curve C at $f \geq 1 \text{ Hz}$ actually originated from the noise level of our measurement electronics (*i.e.*, the preamplifier) rather than from the sample itself. In other words, due to the noise PSD of the preamplifier ($S_V(V_1 = 0) \sim 6 \times 10^{-18} \text{ V}^2/\text{Hz}$), this extracted γ value is really an upper bound rather than an exact value. As expected, our measurements carried out at 2 K (a temperature just above T_c) also indicated that the Hooge constant $\gamma \leq 3 \times 10^{-6}$. Although a low γ value of $\sim 10^{-6}$ was found in semiconductors, such as high-quality GaAs/AlGaAs heterostructures³⁰ and well-annealed doped silicon,³¹ it has not been found in metals or superconductors (in the normal state) except the present epitaxial $\text{CoSi}_2/\text{Si}(100)$ heterostructures. We should emphasize that this upper bound γ value is nearly two (three) orders of magnitudes lower than that of single-crystalline³² (polycrystalline³³) Al films, and eight orders of magnitude lower than that ($\approx 7.7 \times 10^2$) in the high-temperature superconductor $\text{YBa}_2\text{Cu}_3\text{O}_{7-\delta}$ single crystals.³⁴ We mention that this measured value of $\gamma \approx 3 \times 10^{-6}$ is about two orders of magnitude higher than the theoretical estimate of the quantum $1/f$ noise.³⁵ Recall that polycrystalline Al films are an indispensable material widely used in present-day SQUIDs and qubits. Thus, our finding of

the ultralow $1/f$ noise in epitaxial $\text{CoSi}_2/\text{Si}(100)$ heterostructure with $T_c \approx 1.5$ K may likely constitute a feasible substitute for current superconducting devices. Furthermore, it should be reiterated that our choice for using the $\text{Si}(100)$ substrates is readily compatible with existing semiconductor integrated-circuit technology.

In the epitaxial $\text{CoSi}_2/\text{Si}(100)$ heterostructures, the possible origins of the TLSs are unstable interfacial structures and fluctuations of the number of localized charges at the interface/surface. Combining high-resolution XTEM studies, we find that the responsible TLSs are dimer reconstructions and dangling bonds of excess Si atoms residing at the interface (see further discussion below). The amount of these interfacial TLSs governs the total fluctuating scattering cross sections and determines the Hooge γ value. Therefore, we may estimate the TLS density, n_{TLS} , as follows.

The relation between the Hooge parameter γ and the TLS density n_{TLS} is given by³⁶

$$\gamma = \frac{(nl_e\beta\sigma)^2 (n_{\text{TLS}}/n)}{\ln(\omega_{\text{max}}/\omega_{\text{min}})} \quad (2)$$

where $\beta = \delta\sigma/\langle\sigma\rangle$, $\delta\sigma$ denotes the fluctuating scattering cross section, and $\langle\sigma\rangle$ denotes the averaged scattering cross section. ω_{max} and ω_{min} are the upper- and lower-limit frequencies, respectively, of the TLSs. We can rewrite the above equation into the following form

$$\gamma = \frac{\beta^2/e^4}{\ln(\omega_{\text{max}}/\omega_{\text{min}})} \left(n_{\text{TLS}} \frac{(m^*)^2 v_F}{n \rho^2} \sigma^2 \right) \quad (3)$$

Typically, $\beta \approx 0.2$ in real materials.³⁶ The value of $\ln(\omega_{\text{max}}/\omega_{\text{min}})$ can be taken to be approximately the same for all materials due to its logarithmic dependence. Thus, from the known experimental values of $\gamma \approx 1 \times 10^{-3}$ in polycrystalline aluminum^{32,33} and $n_{\text{TLS}} \approx 10^{22} - 10^{24} \text{ m}^{-3}$

in typical polycrystalline metals and alloys,³⁷⁻⁴⁰ we have evaluated a very low TLS density of $n_{\text{TLS}} \approx 10^{18} - 10^{20} \text{ m}^{-3}$ in our epitaxial CoSi₂ films, using the measured upper-bound value of $\gamma \approx 3 \times 10^{-6}$.

We obtain a very small value of $n_{\text{TLS}} \sim 10^{18} - 10^{20} \text{ m}^{-3}$, which is $\sim 10,000$ times lower than that in polycrystalline Al films. In Table 2, we compare the most relevant parameters for epitaxial CoSi₂/Si(100) heterostructures and single-crystalline and polycrystalline Al films grown on SiO₂ or sapphire.^{32,33} The advantages of epitaxial CoSi₂ over Al are evident. An ultra-low level of n_{TLS} immediately suggests the high potential of applying epitaxial CoSi₂ films in high-Q-factor superconducting resonators and superconducting qubits which demand long coherence time. As mentioned, since the charge carriers in our films have a long bulk mean free path, they essentially undergo elastic scattering only at the interface/surface. Therefore, the TLSs in our films, if exist, must most likely be associated with interfacial defects. Then, we may calculate the areal TLS density from the bulk density, *i.e.*, $n_{\text{TLS}_2\text{D}} = n_{\text{TLS}} \times (\text{film thickness}) \approx 10^{11} - 10^{13} \text{ m}^{-2}$. In the case of single crystalline Al films,³² the resistance noise most likely arises from the TLSs residing at the Al/SiO₂ and Al/AlO_x interfaces (a surface AlO_x layer naturally formed in atmosphere), where the value of $n_{\text{TLS}_2\text{D}}$ extracted from Hooge γ is $\sim 3 \times 10^{14} - 3 \times 10^{16} \text{ m}^{-2}$. On the other hand, the $n_{\text{TLS}_2\text{D}}$ value deduced from flux noise measurements on Al/AlO_x-based SQUIDs is $\sim 10^{17} \text{ m}^{-2}$,^{8,9} in satisfactory consistency with the value of $n_{\text{TLS}_2\text{D}}$ from γ . Thus, we can reasonably estimate that, if a SQUID structure is made of CoSi₂/Si and the flux noise measured, the magnitude of $n_{\text{TLS}_2\text{D}}$ to be deduced would be on the order of $\sim 10^{11} - 10^{13} \text{ m}^{-2}$, according to the Hooge γ value given above. Note that such an areal density is 4 to 6 orders of magnitude lower than that ($\sim 10^{17} \text{ m}^{-2}$) in the present-day SQUIDs and qubits made of Al/AlO_x.^{8,9} For the Si(100) plane, the Si density is

$\sim 7 \times 10^{18} \text{ m}^{-2}$. Our $n_{\text{TLS}_{2\text{D}}}$ value thus suggests that only an extremely small fraction of ≤ 1 ppm of the interfacial Si atoms act as TLSs. In the rest of the paper, we elaborate on the TLS picture to analyze and explain in detail the origin for the ultralow noise in epitaxial $\text{CoSi}_2/\text{Si}(100)$ heterostructures.

Table 2. Parameters of epitaxial CoSi_2 and Al.*

| Material | $\rho(300 \text{ K})$ ($\mu\Omega \text{ cm}$) | T_c (K) | Hooge γ | n_{TLS} (m^{-3}) |
|---------------------------|---|--------------|-------------------------|---|
| Epitaxial CoSi_2 | 15 | 1.54 | $\leq 3 \times 10^{-6}$ | $\leq 10^{18} - 10^{20}$ |
| Single-crystalline Al | 2.8 | ~ 1.2 | 1×10^{-4} | $10^{21} - 10^{23}$ |
| Polycrystalline Al | 2.9 | ~ 1.2 | 1×10^{-3} | $10^{22} - 10^{24}$ |

*The Hooge γ values for single-crystalline and polycrystalline Al are taken from refs. 32 and 33, respectively.

At the $\text{CoSi}_2(100)/\text{Si}(100)$ interface, a well-known unstable structure is the 2×1 dimer reconstruction, as previously established by the specific XTEM studies.²³⁻²⁵ In Figure 5(a), the (1) arrows point to the regimes where the interfacial Co atoms are sixfold coordinated with Si by robust covalent bonds.¹³ In this case, the atomic structure is most stable, as schematically depicted by the model in Figure 5(b). On the other hand, the (2) arrow points to a bright atomic cluster where two excess Si atoms can exist. As a consequence, the excess Si atoms can bond to form a dimer which would lower the interfacial energy and reduce the number of dangling bonds (DBs) by half (DBs are schematically depicted by short red dotted lines in Figure 5.) Indeed, this kind of dimer reconstructions at the CoSi_2/Si interface was first found and addressed by Loretto *et al.*²³ (see further discussion on boundary lattice structure in Supporting Information S2). In Figure 5(c) we present a 3D model for the interfacial structure with a dimer (depicted by a red bar in Figure 5). The medium-energy ion scattering studies of the $\text{CoSi}_2/\text{Si}(100)$ interface²⁴ have revealed that

an asymmetric dimer structure, Figures. 5(f) or 5(g), is energetically more favorable than a symmetric structure, the lower panel of Figure 5(d). This situation is reminiscent to that of the well-known buckled dimers on Si(100) surfaces.⁴¹⁻⁴³ The two asymmetric dimer configurations represented in Figures. 5(f) and 5(g) are degenerate and called the θ_0 and $-\theta_0$ states, respectively. In terms of the TLS model, these two states correspond to the two minima of the double-well potential shown in Figure 5(e). Here the $\theta = 0$ state stands for a symmetric dimer, with a potential barrier height V_B . At low temperatures (*e.g.*, close to T_c), the dimer structure will quantum-mechanically switches back and forth between the θ_0 and $-\theta_0$ states,⁴¹⁻⁴⁶ generating an important characteristic energy scale, Δ_0 , between the ground state and the first excited state.

Now we show that the TLS model of Figure 5(e) can well explain the ultralow $1/f$ noise found in this work. Microscopically, when the charge carriers undergo boundary scatterings, where the TLSs reside, the $1/f$ noise is generated. The characteristic switching rate of the buckled dimers at the CoSi₂/Si(100) interface can be evaluated through the well-known relation²⁹

$$\Delta_0 / h = f_0 \cdot \exp(-2\pi d \sqrt{2mV_B} / h) \quad (4)$$

where f_0 is the typical vibrational frequency, m is the mass of the switching object, d is the distance between the two potential minima, and h is the Plank constant. At the CoSi₂/Si interface, $f_0 \sim 1.3 \times 10^{13}$ Hz is the Debye frequency of silicon, m is the mass of Si atom, d is the displacement of flipping Si atoms (~ 0.6 Å for $\theta_0 \approx 15^\circ$ and bond length ≈ 2.3 Å),^{23,42} and $V_B \sim 0.1 - 0.26$ eV for the hole doping circumstance.⁴⁶ With these values, we readily obtain $\Delta_0 / h = 5 \times 10^{-3} - 4 \times 10^3$ Hz. Note that this range of switching rate exactly covers the frequency range for the $1/f$ noise data shown in Figure 4(f). That is, the dimer reconstruction due to excess

Si at the CoSi₂/Si(100) interface is the responsible TLSs. They cause the measured 1/*f* noise. We mention that a similar switching rate of the buckled dimers on Si(100) surface has recently been inferred from the flicker noise in the tunneling current between a scanning tunneling microscopy (STM) tip and a fluctuating dimer.⁴⁴ Apart from the fluctuating dimers discussed above, the remaining dangling bonds (DBs) associated with the excess Si atoms may form another type of TLSs, because the *sp*³ orbitals of Si DBs can act as trapping-detrapping centers for localized charges.^{47,48} However, since in this case the tunneling object is an electron, the typical trapping-detrapping rate ($\Delta_0/h \sim 10^{13}$ Hz)⁴⁸ is too fast to be captured by 1/*f* noise measurements, and thus this process can be ruled out in our case. Thus, we conclude that the fluctuating dimers are the responsible mechanism for generating the 1/*f* noise in epitaxial CoSi₂/Si(100) heterostructures. The magnitude of the noise is ultralow because we have an extremely low areal (dimer) density of $n_{\text{TLS}_{2\text{D}}} = 10^{11} - 10^{13} \text{ m}^{-2}$. The areal density of the remaining DBs must be also on the same order, because there are two remaining DBs per dimer. For comparison, we should note that, in present-day Al/AIO_x-based superconducting qubit devices, large amounts of trapped charges in DBs in the dielectric regime often generate notoriously high levels of 1/*f* noise.⁷⁻⁹

CONCLUSION

In summary, we have found ultralow 1/*f* noise in a heterostructure of superconducting epitaxial CoSi₂ thin film on Si(100). The noise level is 2 to 3 orders of magnitude lower than that in Al, while a sharp superconducting transition occurs at a manageably high temperature of 1.5 K. The microscopic origin for the ultralow 1/*f* noise is ascribed to the dimer reconstruction at the CoSi₂/Si(100) interface. The areal density of fluctuating dimers was evaluated and found to be 4 to 6 orders of magnitude lower than those in the widespread superconducting qubit devices made of Al/AIO_x. While preparing an epitaxial dielectric barrier in Al/Al₂O₃-based structures to reduce

the $1/f$ noise level is nontrivial,^{6,49,50} it is highly workable to utilize single-crystalline, undoped Si as an epitaxial dielectric layer, sandwiching it between two CoSi_2 films to form a (lateral) Josephson junction or SQUID with a one-step lithographic process. One can then study the flux noise spectra of a CoSi_2/Si -based SQUID to justify the low noise property. In addition, measurements of the relaxation time T_1 should be performed to check if any source(s) for high-frequency relaxation are rare. Another study can be done is to make a superconducting coplanar waveguide using epitaxial CoSi_2/Si to check whether it has a high Q-factor. Although the $1/f$ noise issues can be minimized in certain qubit designs,^{51,52} the noisy superconducting components still exist in other parts of superconducting devices and play an important role in determining the performance of the whole devices/circuits.

It should be stressed that the $1/f$ noise level will hinder the performance of the ultra-sensitive magnetic field sensors based on SQUIDs, where the sensitivity cannot be improved by increasing the measurement time.^{53,54} Thus, a very low $1/f$ noise level for the superconducting materials and qubits is definitely required. At present, the bottleneck for superconducting circuit-based quantum computing lies at the fourth stage, where the critical difficulty is how to maintain sufficiently long lifetime for logical quantum memory.³ We propose to use the excellent epitaxial properties of CoSi_2/Si to minimize decoherence sources at the surfaces and interfaces, and hence increase the coherence time for breaking through the fourth stage. Note that the fabrication processes for CoSi_2/Si devices are readily compatible with the present-day silicon-based technology. These new-generation CoSi_2/Si -based devices may be exploited as potential substitutes for the current Al/AlO_x -based devices.

METHODS

Sample Preparation. Epitaxial CoSi₂/Si(100) heterostructures. A 30 nm thick Co film was first deposited *via* thermal evaporation on a native oxide removed lightly boron-doped (*p*-type) Si(100) substrate. The Co/Si specimen was subsequently annealed at 800°C in a high vacuum of 1×10^{-5} torr for 30, 60 or 90 min. Such extended annealing time periods, as compared with the rapid thermal processes (RTP) commonly used in the CMOS production,^{12,15,55} ensured complete reaction of the deposited cobalt atoms with substrate Si atoms. The thickness of the CoSi₂ film thus formed was ≈ 105 nm, in good agreement with previous finding.⁵⁵ By employing three periods of annealing time, we were able to examine various stages of the phase formation and morphology at the CoSi₂/Si interface.

Non-epitaxial CoSi₂ films. For comparison, we also grew non-epitaxial CoSi₂ films and studied their structural, electrical and noise properties. A Co/Si/Co/Si/Co/Si multilayer was first deposited on a 300-nm SiO₂ capped Si substrate *via* thermal evaporation, where each Co (Si) layer was 10 (36) nm thick. This thickness ratio of 1:3.6 facilitated the formation of a stoichiometric CoSi₂ film when the multilayer was annealed in a high vacuum at 800°C for 90 min. The as-grown films were polycrystalline, with a grain size of ≈ 10 nm. The CoSi₂/SiO₂ interface did not reveal any epitaxial relations, as evidenced from XTEM studies.

High-Resolution Cross-Sectional Transmission Electron Microscopy (XTEM) Studies. The XTEM studies of our films were carried out using a spherical aberration corrected scanning transmission electron microscope (JEOL ARM200F).

Electrical-Transport Measurements. The resistivity $\rho(T)$ of our CoSi₂ films was measured using an ac resistance bridge (Linear Research LR700 or LR400) with the four-probe configuration in an Oxford Heliox ³He cryostat. The T_c value was determined by the 50% drop of the normal-

state resistance, R_N . The superconducting transition width ΔT_c was defined by the temperature difference between the 10% and 90% drops of R_N . The T_c and ΔT_c values are listed in Table 1.

Low-Frequency Noise Measurements. The $1/f$ noise of our films was measured with an ac bridge technique using the five-terminal configuration,^{56,57} Figure 4(a). The CoSi_2 films were patterned by the electron-beam lithography technique to have typical dimensions of $\approx 50 \mu\text{m}$ long and $\approx 0.8 \mu\text{m}$ wide. The electrodes were made of Ti/Au (15/65 nm) *via* thermal evaporation. Two current leads (I_1 and I_2) were respectively connected to two variable resistors (R_1 and R_2), while two voltage leads (V_1 and V_2) were connected to the input of a preamplifier operating in the differential mode. The resistances for the two CoSi_2 segments were approximately equal ($r_{s1} \approx r_{s2}$). The two variable resistors were tuned to balance the two voltages V_1 and V_2 . When the bridge was in balance, the average voltage drop $\langle \delta V \rangle \approx \langle V_1 - V_2 \rangle$ was minimized so that the higher gain of the preamplifier could be utilized to amplify the signal against the contingent noise in the following stages. The balance of the bridge also eliminated the noise contribution from the voltage fluctuations of the power supply and the contact resistance in the central terminal. In our measurements, the unbalance ratio was $\langle \delta V \rangle / \langle V_1 \rangle \approx 4 \times 10^{-4} - 1 \times 10^{-2}$ for all samples. A sinusoidal driving voltage was used to modulate the low frequency signal of our samples to an optimal frequency ($\approx 3.1 \text{ kHz}$) of the preamplifier (Stanford SR560), where the $1/f$ noise from the preamplifier was minimized. The amplified signal was thus demodulated using the phase-sensitive-detecting technique to retrieve the $1/f$ signal of the sample. The retrieved signal was digitalized by a lock-in amplifier (Stanford SR830) with a rate of 512 Hz and recorded by a spectrum analyzer (Stanford SR785). Throughout measurements, we set $R_i > 10r_{si}$ ($i = 1, 2$). Typical sets of raw data are shown in Figures. 4(b) and 4(d).

ASSOCIATED CONTENT

Supporting Information: Superconducting transition and magnetoresistance for CoSi₂/Si(100) heterostructures; Assignment of atomic positions and atomic model for the CoSi₂/Si(100) interface. This material is available free of charge *via* the Internet at <http://pubs.acs.org>.

AUTHOR INFORMATION

Corresponding Author

*Email: ycchou@nctu.edu.tw

*Email: jjlin@mail.nctu.edu.tw

Author Contributions

S.P.C. synthesized the samples and carried out transport characterizations, S.S.Y. performed $1/f$ noise measurements, C.J.C. and Y.C.C. carried out TEM studies, J.J.L. and C.C.T. supervised the work. All authors participate in the discussion and interpretation of the results and co-write the manuscript.

Notes

The authors declare no competing financial interests.

ACKNOWLEDGMENT

The authors thank Ruey-Tay Wang for experimental assistance of $1/f$ noise measurements. This work was supported by the Taiwan Ministry of Science and Technology (MOST) through Grant numbers MOST-103-2112-M-009-017-MY3, 105-2923-M-009-005-MY2 (J.J.L.), and MOST-104-2112-M-009-015-MY3 (Y.C.C), and the Taiwan Ministry of Education (MOE) ATU Plan.

REFERENCES

1. Clarke, J.; Wilhelm, F. K. Superconducting Quantum Bits. *Nature* **2008**, *453*, 1031-1042.
2. You, J. Q.; Nori, F. Superconducting Circuits and Quantum Information. *Phys. Today* **2005**, *58*, 42-47.
3. Devoret, M. H.; Schoelkopf, R. J. Superconducting Circuits for Quantum Information: An Outlook. *Science* **2013**, *339*, 1169-1174.
4. Oliver, W. D.; Welander, P. B. Materials in Superconducting Quantum Bits. *MRS Bull.* **2013**, *38*, 816-825.
5. Fowler, A. G.; Mariantoni, M.; Martinis, J. M.; Cleland, A. N. Surface Codes: Towards Practical Large-Scale Quantum Computation. *Phys. Rev. A* **2012**, *86*, 032324.
6. Martinis, J. M.; Megrant, A. UCSB Final Report for the CSQ Program: Review of Decoherence and Materials Physics for Superconducting Qubits. 2014, arXiv:1410.5793 [quant-ph]. arXiv.org e-Print archive. <https://arxiv.org/abs/1410.5793> (accessed Nov 17, 2015).
7. Paladino, E.; Galperin, Y. M.; Falci, G.; Altshuler, B. L. $1/f$ Noise: Implications for Solid-State Quantum Information. *Rev. Mod. Phys.* **2014**, *86*, 361-418.
8. Koch, R. H.; DiVincenzo, D. P.; Clarke, J. Model for $1/f$ Flux Noise in SQUIDs and Qubits. *Phys. Rev. Lett.* **2007**, *98*, 267003.
9. Choi, S.; Lee, D.-H.; Louie, S. G.; Clarke, J. Localization of Metal-Induced Gap States at the Metal-Insulator Interface: Origin of Flux Noise in SQUIDs and Superconducting Qubits. *Phys. Rev. Lett.* **2009**, *103*, 197001.
10. Hensel, J. C.; Tung, R. T.; Poate, J. M.; Unterwald, F. C. Specular Boundary Scattering and Electrical Transport in Single-Crystal Thin Films of CoSi_2 . *Phys. Rev. Lett.* **1985**, *54*, 1840-1843.
11. Matthias, B. T.; Hulm, J. K. Superconducting Properties of Cobalt Disilicide. *Phys. Rev.* **1953**, *89*, 439-441.
12. Chen, L. J.; Tu, K. N. Epitaxial Growth of Transition-Metal Silicides on Silicon. *Mater. Sci. Rep.* **1991**, *6*, 53-140.
13. Dézsi, I.; Engelmann, H.; Gonser, U.; Langouche, G. Cobalt-Silicide Structures Studied by Mössbauer Spectroscopy. *Hyperfine Interact.* **1987**, *33*, 161-171.
14. Radermacher, K.; Monroe, D.; White, A. E.; Short, K. T.; Jevasinski, R. Quantum Transport of Buried Single-Crystalline CoSi_2 Layers in (111)Si and (100)Si Substrates. *Phys. Rev. B: Condens. Matter Mater. Phys.* **1993**, *48*, 8002-8015.
15. Reader, A. H.; Ommen, A. H. v.; Weijs, P. J. W.; Wolters, R. A. M.; Oostra, D. J. Transition Metal Silicides in Silicon Technology. *Rep. Prog. Phys.* **1993**, *56*, 1397.
16. Chou, Y.-C.; Lu, K.-C.; Tu, K. N. Nucleation and Growth of Epitaxial Silicide in Silicon Nanowires. *Mater. Sci. Eng., R* **2010**, *70*, 112-125.

17. Weiß, W.; Starke, U.; Heinz, K.; Rangelov, G.; Fauster, T.; Castro, G. R. LEED Structure Determination of the (100)-Surface of a CoSi₂ Crystal and a CoSi₂ Film Grown Epitaxially on Si(100). *Surf. Sci.* **1996**, *347*, 117-127.
18. Voigtländer, B.; Scheuch, V.; Bonzel, H. P.; Heinze, S.; Blügel, S. Chemical Identification of Atoms at Multicomponent Surfaces on an Atomic Scale: CoSi₂(100). *Phys. Rev. B: Condens. Matter Mater. Phys.* **1997**, *55*, R13444-R13447.
19. Chiou, C.-J.; Chiu, S.-P.; Lin, J.-J.; Chou, Y.-C. Effects of Atomic Scale Imperfection at the Interfaces of CoSi₂ and Si (100) on Schottky Barrier Contacts. *CrystEngComm* **2015**, *17*, 4276-4280.
20. White, A. E.; Short, K. T.; Dynes, R. C.; Garno, J. P.; Gibson, J. M. Mesotaxy: Single-Crystal Growth of Buried CoSi₂ Layers. *Appl. Phys. Lett.* **1987**, *50*, 95-97.
21. Van Ommen, A. H.; Bulle-Lieuwma, C. W. T.; Ottenheim, J. J. M.; Theunissen, A. M. L. Ion Beam Synthesis of Heteroepitaxial Si/CoSi₂/Si Structures. *J. Appl. Phys.* **1990**, *67*, 1767-1778.
22. Bulle-Lieuwma, C. W. T.; van Ommen, A. H.; Hornstra, J.; Aussems, C. N. A. M. Observation and Analysis of Epitaxial Growth of CoSi₂ on (100) Si. *J. Appl. Phys.* **1992**, *71*, 2211-2224.
23. Loretto, D.; Gibson, J. M.; Yalisove, S. M. Evidence for a Dimer Reconstruction at a Metal-Silicon Interface. *Phys. Rev. Lett.* **1989**, *63*, 298-301.
24. Copel, M.; Falta, J. Frustrated Dimers at the CoSi₂/Si(001) Interface. *Phys. Rev. B: Condens. Matter Mater. Phys.* **1993**, *48*, 2783-2786.
25. Yu, B. D.; Miyamoto, Y.; Sugino, O.; Sakai, A.; Sasaki, T.; Ohno, T. Structural and Electronic Properties of Metal-Silicide/Silicon Interfaces: A First-Principles Study. *J. Vac. Sci. Technol., B* **2001**, *19*, 1180-1185.
26. Buschmann, V.; Rodewald, M.; Fuess, H.; Van Tendeloo, G.; Schäffer, C. Hetero-Epitaxial Growth of CoSi₂ Thin Films on Si(100): Template Effects and Epitaxial Orientations. *J. Cryst. Growth* **1998**, *191*, 430-438.
27. Falke, M.; Falke, U.; Bleloch, A.; Teichert, S.; Beddies, G.; Hinneberg, H.-J. Real Structure of the CoSi₂/Si(001) Interface Studied by Dedicated Aberration-Corrected Scanning Transmission Electron Microscopy. *Appl. Phys. Lett.* **2005**, *86*, 203103.
28. Dutta, P.; Horn, P. M. Low-Frequency Fluctuations in Solids: 1/f Noise. *Rev. Mod. Phys.* **1981**, *53*, 497-516.
29. Weissman, M. B. 1/f Noise and Other Slow, Nonexponential Kinetics in Condensed Matter. *Rev. Mod. Phys.* **1988**, *60*, 537-571.
30. Tacano, M. Hooge Fluctuation Parameter of Semiconductor Microstructures. *IEEE Trans. Electron Devices* **1993**, *40*, 2060-2064.
31. Vandamme, L. K. J.; Oosterhoff, S. Annealing of Ion-Implanted Resistors Reduces the 1/f Noise. *J. Appl. Phys.* **1986**, *59*, 3169-3174.

32. van den Homberg, M. J. C.; Verbruggen, A. H.; Alkemade, P. F. A.; Radelaar, S.; Ochs, E.; Armbruster-Dagge, K.; Seeger, A.; Stoll, H. $1/f$ Noise in Mono- and Polycrystalline Aluminum. *Phys. Rev. B: Condens. Matter Mater. Phys.* **1998**, *57*, 53-55.
33. Scofield, J. H.; Mantese, J. V.; Webb, W. W. $1/f$ Noise of Metals: A Case for Extrinsic Origin. *Phys. Rev. B: Condens. Matter Mater. Phys.* **1985**, *32*, 736-742.
34. Song, Y.; Misra, A.; Crooker, P. P.; Gaines, J. R. $1/f$ Noise and Morphology of $\text{YBa}_2\text{Cu}_3\text{O}_{7-\delta}$ Single Crystals. *Phys. Rev. Lett.* **1991**, *66*, 825-828.
35. Handel, P. H. Quantum Approach to $1/f$ Noise. *Phys. Rev. A* **1980**, *22*, 745-757.
36. Feng, S. Conductance Fluctuations and $1/f$ Noise Magnitudes in Small Disordered Structures: Theory. In *Mesoscopic Phenomena in Solids*, Al'tshuler, B. L.; Lee, P. A.; Webb, R. A., Eds. Elsevier: Amsterdam, 1991; pp 107-129.
37. Lien, A.-S.; Wang, L. Y.; Chu, C. S.; Lin, J.-J. Temporal Universal Conductance Fluctuations in RuO_2 Nanowires due to Mobile Defects. *Phys. Rev. B: Condens. Matter Mater. Phys.* **2011**, *84*, 155432.
38. Chiu, S.-P.; Chung, H.-F.; Lin, Y.-H.; Kai, J.-J.; Chen, F.-R.; Lin, J.-J. Four-Probe Electrical-Transport Measurements on Single Indium Tin Oxide Nanowires Between 1.5 and 300 K. *Nanotechnology* **2009**, *20*, 105203.
39. Birge, N. O.; Golding, B.; Haemmerle, W. H. Conductance Fluctuations and $1/f$ Noise in Bi. *Phys. Rev. B: Condens. Matter Mater. Phys.* **1990**, *42*, 2735-2743.
40. Chun, K.; Birge, N. O. Dissipative Quantum Tunneling of a Single Defect in a Disordered Metal. *Phys. Rev. B: Condens. Matter Mater. Phys.* **1996**, *54*, 4629-4637.
41. Chadi, D. J. Atomic and Electronic Structures of Reconstructed Si(100) Surfaces. *Phys. Rev. Lett.* **1979**, *43*, 43-47.
42. Ihm, J.; Cohen, M. L.; Chadi, D. J. (2×1) Reconstructed Si(001) Surface: Self-Consistent Calculations of Dimer Models. *Phys. Rev. B: Condens. Matter Mater. Phys.* **1980**, *21*, 4592-4599.
43. Tromp, R. M.; Hamers, R. J.; Demuth, J. E. Si(001) Dimer Structure Observed with Scanning Tunneling Microscopy. *Phys. Rev. Lett.* **1985**, *55*, 1303-1306.
44. Hata, K.; Sainoo, Y.; Shigekawa, H. Atomically Resolved Local Variation of the Barrier Height of the Flip-Flop Motion of Single Buckled Dimers of Si(100). *Phys. Rev. Lett.* **2001**, *86*, 3084-3087.
45. Yokoyama, T.; Takayanagi, K. Anomalous Flipping Motions of Buckled Dimers on the Si(001) Surface at 5 K. *Phys. Rev. B: Condens. Matter Mater. Phys.* **2000**, *61*, R5078-R5081.
46. Ren, X.-Y.; Kim, H.-J.; Niu, C.-Y.; Jia, Y.; Cho, J.-H. Origin of Symmetric Dimer Images of Si(001) Observed by Low-Temperature Scanning Tunneling Microscopy. *Sci. Rep.* **2016**, *6*, 27868.
47. Campbell, J. P.; Lenahan, P. M. Density of States of Pb1 Si/SiO₂ Interface Trap Centers. *Appl. Phys. Lett.* **2002**, *80*, 1945-1947.

48. Schofield, S. R.; Studer, P.; Hirjibehedin, C. F.; Curson, N. J.; Aeppli, G.; Bowler, D. R. Quantum Engineering at the Silicon Surface Using Dangling Bonds. *Nat. Commun.* **2013**, *4*, 1649.
49. Oh, S.; Cicak, K.; Kline, J. S.; Sillanpää, M. A.; Osborn, K. D.; Whittaker, J. D.; Simmonds, R. W.; Pappas, D. P. Elimination of Two Level Fluctuators in Superconducting Quantum Bits by an Epitaxial Tunnel Barrier. *Phys. Rev. B: Condens. Matter Mater. Phys.* **2006**, *74*, 100502.
50. Weides, M. P.; Kline, J. S.; Vissers, M. R.; Sandberg, M. O.; Wisbey, D. S.; Johnson, B. R.; Ohki, T. A.; Pappas, D. P. Coherence in a Transmon Qubit with Epitaxial Tunnel Junctions. *Appl. Phys. Lett.* **2011**, *99*, 262502.
51. Paik, H.; Schuster, D. I.; Bishop, L. S.; Kirchmair, G.; Catelani, G.; Sears, A. P.; Johnson, B. R.; Reagor, M. J.; Frunzio, L.; Glazman, L. I.; *et al.* Observation of High Coherence in Josephson Junction Qubits Measured in a Three-Dimensional Circuit QED Architecture. *Phys. Rev. Lett.* **2011**, *107*, 240501.
52. Rigetti, C.; Gambetta, J. M.; Poletto, S.; Plourde, B. L. T.; Chow, J. M.; Córcoles, A. D.; Smolin, J. A.; Merkel, S. T.; Rozen, J. R.; Keefe, G. A.; *et al.* Superconducting Qubit in a Waveguide Cavity with a Coherence Time Approaching 0.1 ms. *Phys. Rev. B: Condens. Matter Mater. Phys.* **2012**, *86*, 100506.
53. Balandin, A. A. Low-Frequency $1/f$ Noise in Graphene Devices. *Nat. Nanotechnol.* **2013**, *8*, 549-555.
54. Pettai, R. *Noise in Receiving Systems*. Wiley: New York, 1984.
55. Kikkawa, T.; Inoue, K.; Imai, K. Cobalt Silicide Technology. In *Silicide Technology for Integrated Circuits*, Chen, L. J., Ed. The Institution of Engineering and Technology: London, 2004; pp 77 - 94.
56. Scofield, J. H. Ac Method for Measuring Low-Frequency Resistance Fluctuation Spectra. *Rev. Sci. Instrum.* **1987**, *58*, 985-993.
57. Yeh, S.-S.; Hsu, W.-M.; Lee, J.-K.; Lee, Y.-J.; Lin, J.-J. $1/f$ Noise in Micrometer-Sized Ultrathin Indium Tin Oxide Films. *Appl. Phys. Lett.* **2013**, *103*, 123118.

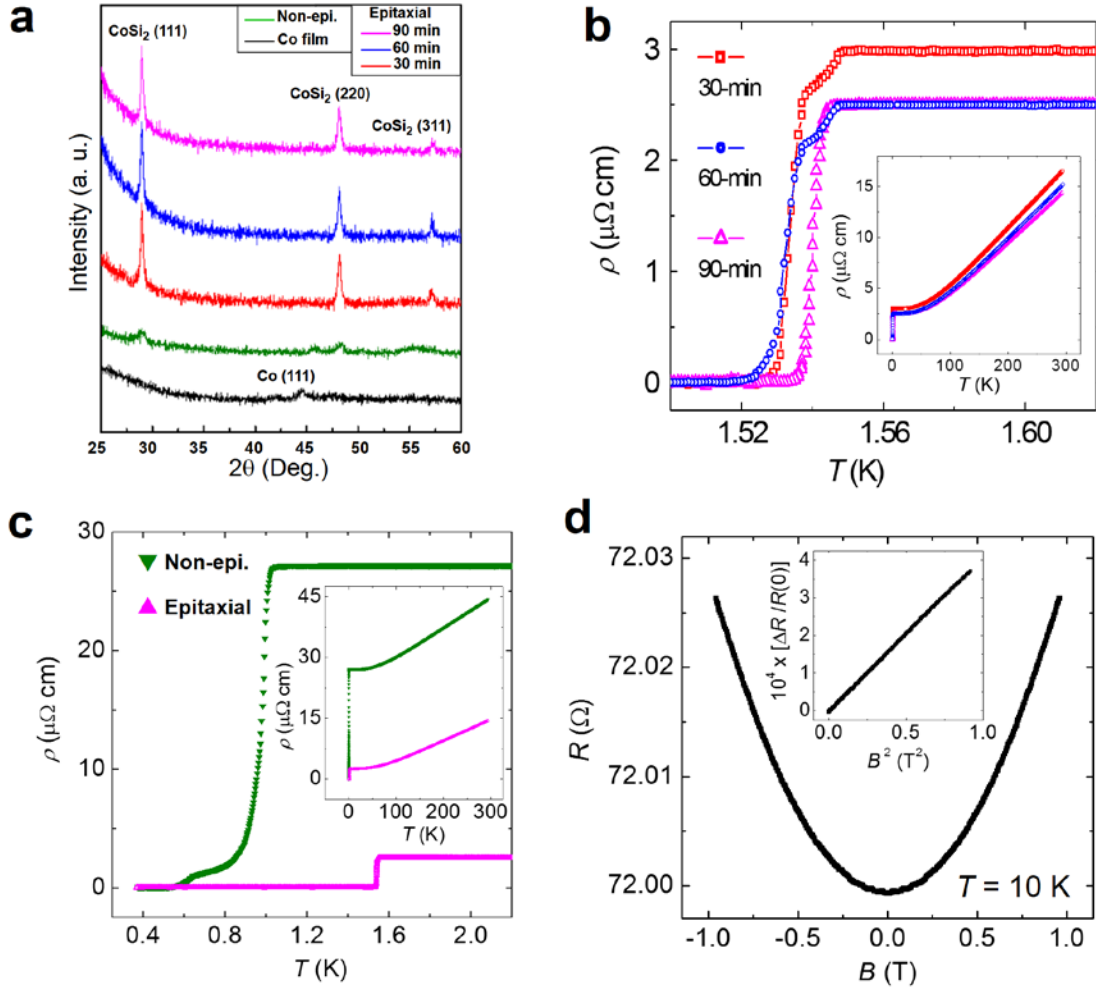


Figure 1. Grazing x-ray diffraction (GIXRD) spectra, cross-sectional TEM (XTEM) images, superconducting transitions, and magnetoresistance (MR) of CoSi₂ films. (a) GIXRD spectra for 30, 60 and 90 min annealed epitaxial CoSi₂ films, as indicated. The film thickness is ≈ 105 nm. The spectra for a non-epitaxial CoSi₂ and a pure Co films are also shown for comparison. (b) Superconducting transitions for three epitaxial CoSi₂ films, as indicated. The 90 min annealed film undergoes a very sharp superconducting transition at 1.54 K, with a narrow transition width of 5 mK. The inset shows the variation of resistivity with temperature between 1 and 300 K for the two films. (c) Superconducting transitions for a non-epitaxial and an epitaxial CoSi₂ films, as indicated. Inset: temperature dependence of resistivity between 1 and 300 K for the two films. (d) MR for a 90 min annealed epitaxial CoSi₂ film at $T = 10$ K. The inset shows that the normalized MR is proportional to the square of magnetic field.

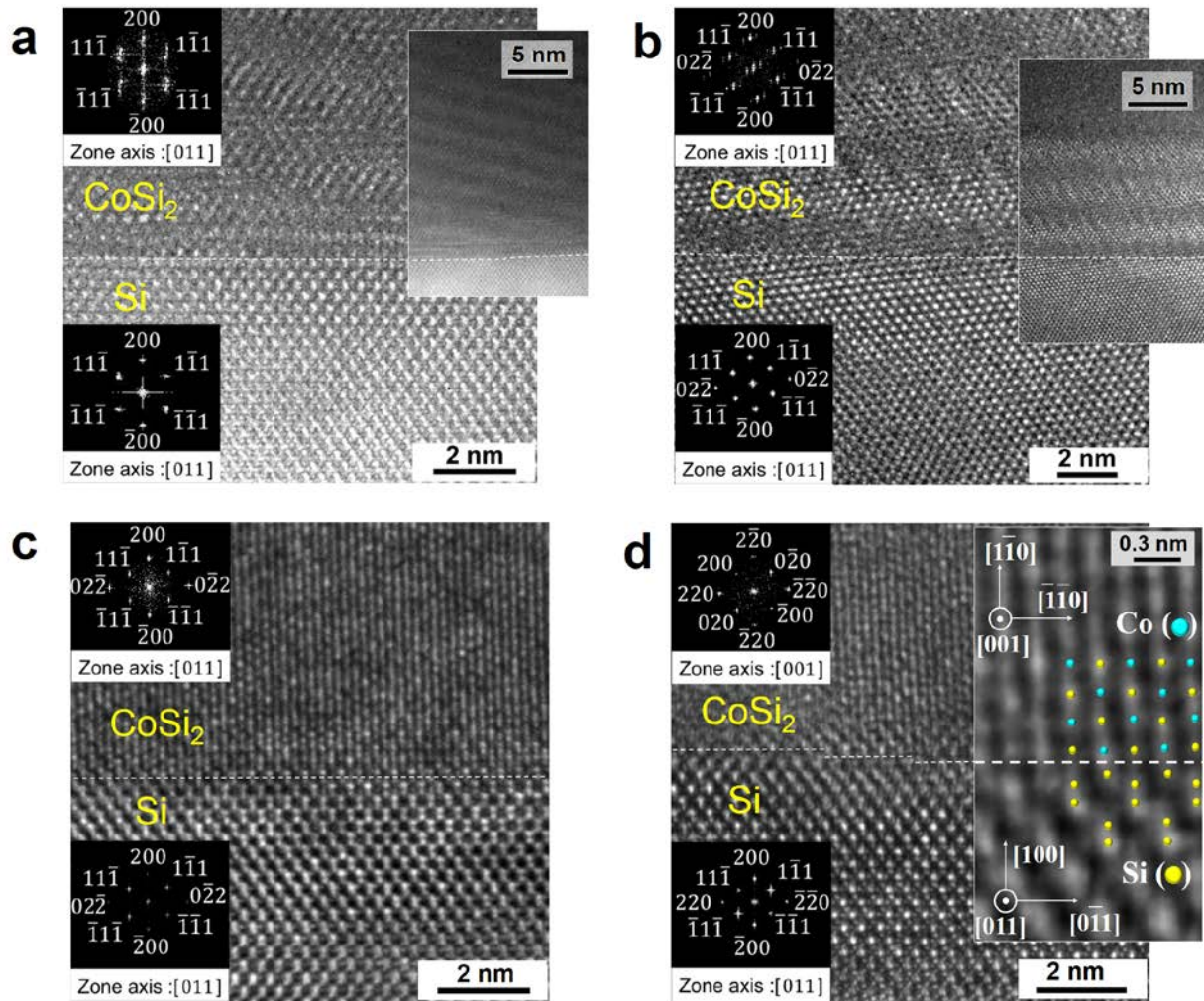


Figure 2. (a)–(d) show the XTEM images for 30, 60, 90 and 90 min annealed epitaxial CoSi_2 films, respectively. In each figure, the dashed line indicates the CoSi_2 and Si phase boundary, and the left insets show the diffraction patterns for (top) CoSi_2 and (bottom) Si(100). The right insets in (a) and (b) show XTEM images for Moiré fringes. The right inset in (d) shows a zoom-in image for the epitaxy of $\text{CoSi}_2(110)$ on Si(100), highlighted with blue (Co) and yellow (Si) balls.

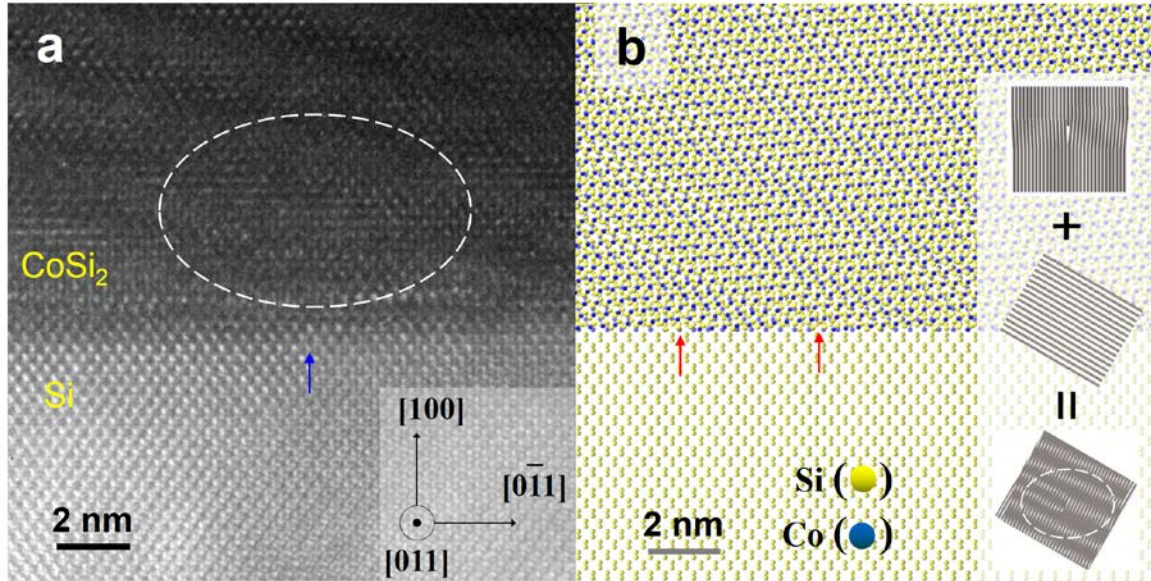


Figure 3. (a) XTEM image of a 30 min annealed sample. Moiré fringes on the CoSi_2 side are evident. (b) Corresponding atomic simulations for the image of Moiré fringes shown in (a). The inset shows a schematic for a distorted Moiré fringe due to the existence of an edge dislocation combined with a rotational shift between two sets of CoSi_2 lattice. The arrows in (a) and (b) indicate three interfacial locations with notable atomic misfits at the CoSi_2 - Si boundary.

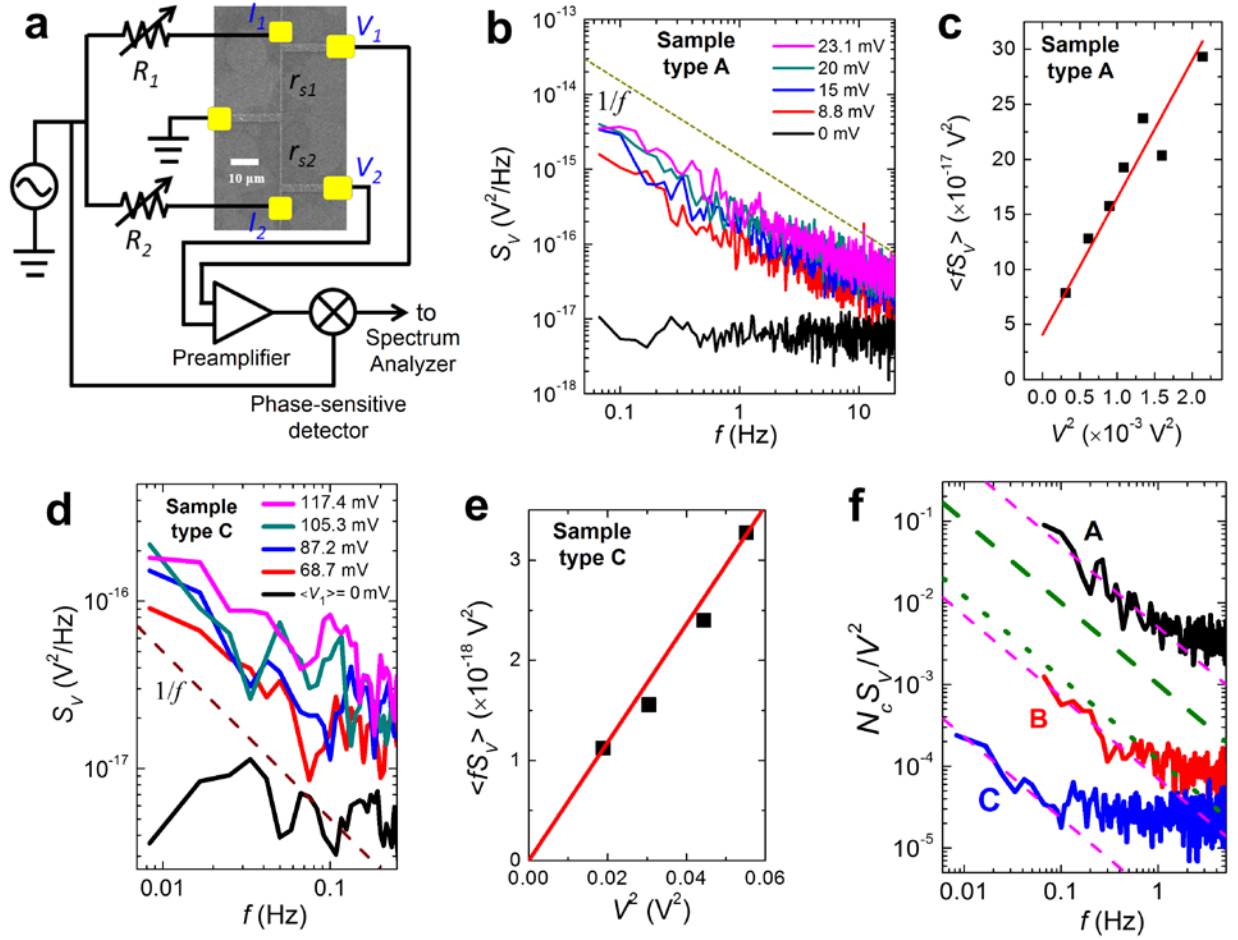


Figure 4. (a) A schematic for $1/f$ noise measurement setup. The five-terminal CoSi_2 sample ($0.8 \mu\text{m}$ wide and $\approx 105 \text{ nm}$ thick) was fabricated *via* electron-beam lithography. The yellow regions schematically depict Ti/Au patterns on CoSi_2 as electrodes and wire-bonding pads. (b) and (d) are the voltage power spectrum densities (PSD) of samples type A and type C, respectively, under various bias voltages as indicated. The dashed lines are drawn proportional to $1/f$ and is a guide for the eye. The $\langle fS_V \rangle$ values are calculated from the $1/f$ dependent regime and plotted as a function of V^2 for samples type A and type C in (c) and (e), respectively. The straight lines are linear fits. (f) Normalized voltage noise PSD for three types of samples measured at 150 K: sample type A (C) is an epitaxial CoSi_2 film without (with) HF treatment of the CoSi_2 top surface before depositing Ti/Au electrodes, and sample type B is a non-epitaxial CoSi_2 film with HF treatment. The normalized noise PSDs for a polycrystalline Al film at 300 K (green dashed line) (taken from ref. 32), and a single-crystalline Al film at 150 K (green dotted line) (taken from ref. 33) are plotted

for comparison. The dashed and dotted lines indicate $1/f$ frequency dependence. The data of sample type C suggests an ultralow Hooge parameter $\gamma \leq 3 \times 10^{-6}$ for the epitaxial $\text{CoSi}_2/\text{Si}(100)$ heterostructure.

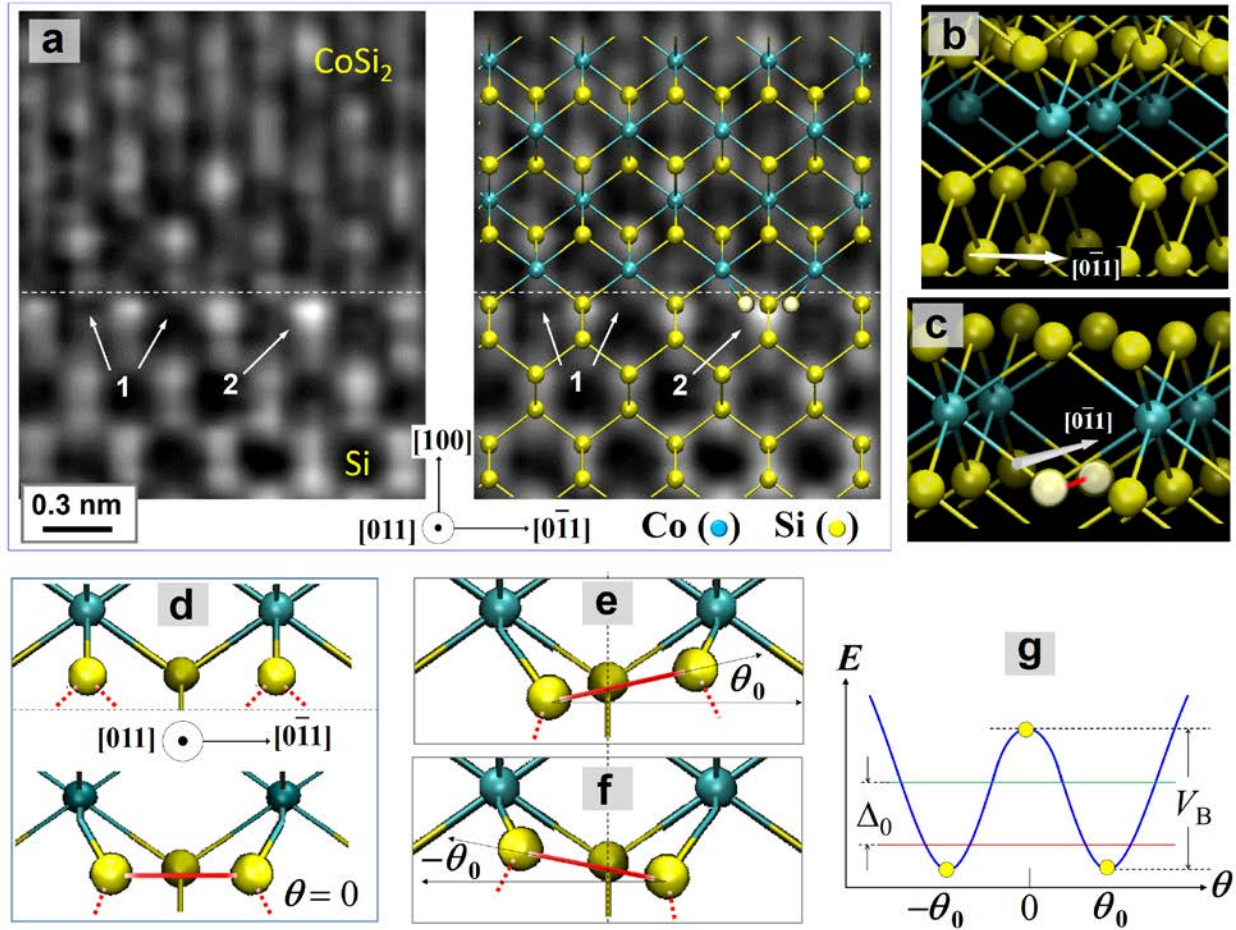
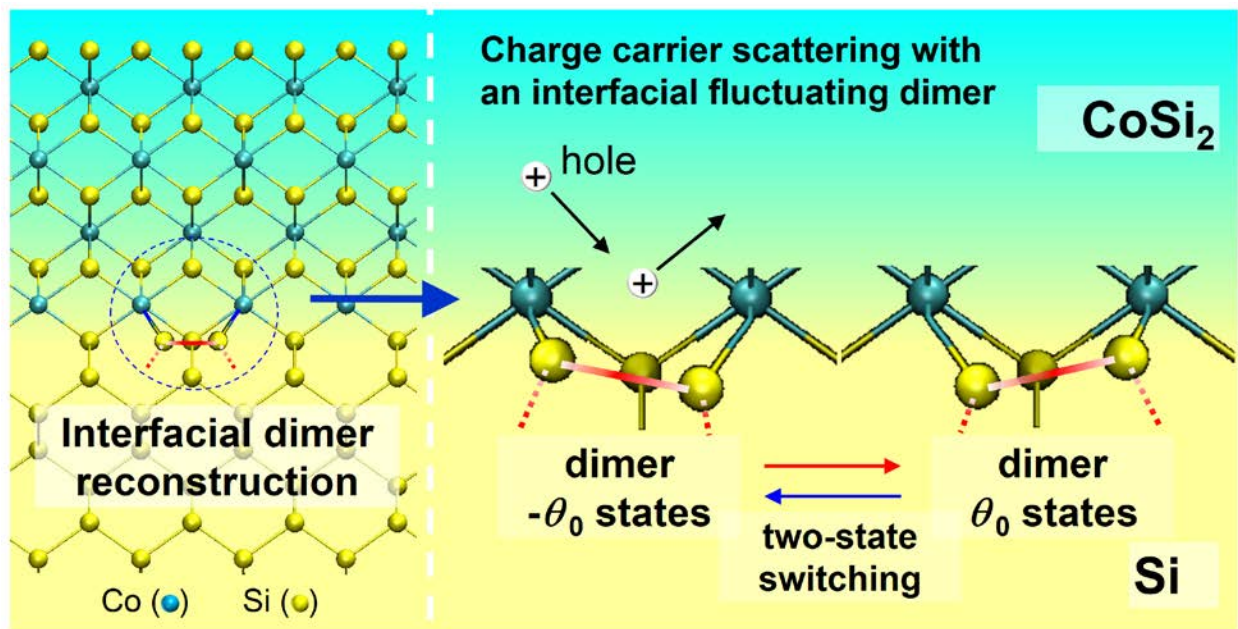


Figure 5. XTEM images and schematic diagrams depicting two-level system models for fluctuating dimers. (a) Left panel: XTEM image with epitaxy of $\text{CoSi}_2(100)$ on $\text{Si}(100)$ taken from a portion of Figure 2(c). Right panel: the same image with the mapping of a ball-and-stick model projected on the (011) plane. The region enclosed by (1) arrows can be modeled with sixfold coordinated Co, as shown in (b). The regions enclosed by (2) arrows can be modeled with a dimer reconstruction (red bar), as shown in (c). The upper panel in (d) depicts a model without a dimer reconstruction. The lower panel of (d), (f) and (g) depict symmetric ($\theta_0 = 0$) and buckled ($\theta_0, -\theta_0$) dimers, respectively. In the double-well potential shown in (e), the two minima represent the buckled dimer states, and the top of barrier height V_B represents the symmetric dimer state.

Table of Contents Graphic:



Supplementary Material:

Ultralow $1/f$ Noise in a Heterostructure of Superconducting Epitaxial Cobalt-Disilicide Thin Film on Silicon

Shao-Pin Chiu,[†] Sheng-Shiuan Yeh,[†] Chien-Jyun Chiou,[‡] Yi-Chia Chou,^{*,‡} Juhn-Jong Lin,^{*,†,‡} and Chang-Chyi Tsuei[§]

[†]Institute of Physics, National Chiao Tung University, Hsinchu 300, Taiwan

[‡]Department of Electrophysics, National Chiao Tung University, Hsinchu 300, Taiwan

[§]IBM Thomas J. Watson Research Center Yorktown Heights, NY 10598, U.S.A.

*Email: ycchou@nctu.edu.tw

*Email: jjlin@mail.nctu.edu.tw

S1. Superconducting transition and magnetoresistance for $\text{CoSi}_2/\text{Si}(100)$ heterostructures

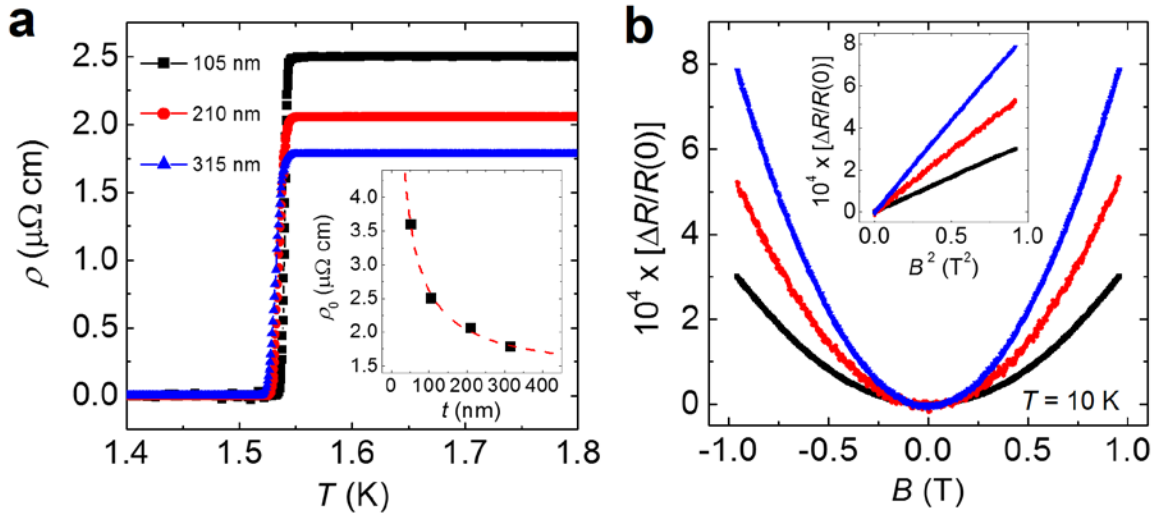


Fig. S1 (a) Resistivity as a function of temperature around superconducting transitions for three CoSi_2 films, as indicated. Inset: variation of residual resistivity with film thickness. (b) Normalized magnetoresistances for 105, 210, and 315 nm thick CoSi_2 films, as indicated. The data for the 105 nm, 90 min annealed CoSi_2 film (black curves) are also plotted in the Figs. 1(b) and 1(d) in the manuscript.

We have carried out additional electrical and magneto-transport measurements on 53, 210 and 315 nm thick CoSi_2 films on $\text{Si}(100)$. Figure S1(a) shows very sharp superconducting transitions for three representative films, suggesting excellent sample quality. The inset shows the variation of residual resistivity ρ_0 with film thickness t . The decrease of ρ_0 with increasing t implies that boundary scattering still plays a role even in our thickest film. By least-squares fitting

to the Fuchs-Sondheimer theory [1,2] (the red dashed curve) as previously done by Hensel, *et al.* [3], we obtained the following parameters: bulk resistivity $\rho_{0,bulk} \approx 1.48 \mu\Omega \text{ cm}$, bulk elastic mean free path $l_{e,bulk} \approx 363 \text{ nm}$, and scattering specularity $p \approx 0.45$. This $l_{e,bulk}$ value is close to the grain size in the lateral directions in our 105 nm CoSi₂ films, as mentioned in the manuscript.

Figure S1(b) shows that the magnitude of the normalized magnetoresistance (MR), $\Delta R / R(0) \approx (\mu B)^2$, increases with increasing film thicknesses, suggesting higher mobility μ in thicker films. Using the extracted μ values and following the calculation procedure described in the manuscript, we obtained $l_e \approx 121, 142$ and 175 nm in the 105, 210 and 315 nm thick films, respectively. This thickness dependent l_e value implies and supports a relatively long $l_{e,bulk} \approx 363 \text{ nm}$ mentioned above. Thus, for the 105 nm thick CoSi₂ films studied in this work, boundary scattering dominates the electrical transport. This result confirms that the measured $1/f$ noise originates from TLS fluctuators at interface.

S2. Assignment of atomic positions and atomic model for the CoSi₂/Si(100) interface

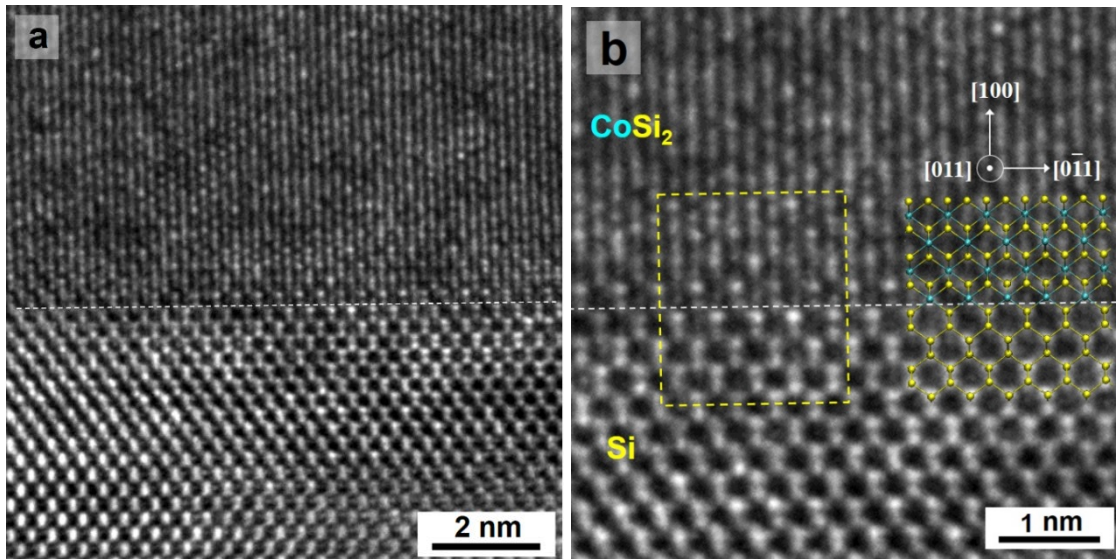


Fig. S2 Cross-sectional HRTEM images for 90 min annealed CoSi₂/Si sample. **(a)** The field size is $\approx 10 \times 10 \text{ nm}^2$. The dashed line indicates the CoSi₂-Si boundary. **(b)** An enlarged image of (a). The field size is $\approx 5 \times 5 \text{ nm}^2$.

We describe step by step how we identify the atomic positions at the CoSi₂/Si interface from the HRTEM image. Figure S2(a) shows a cross-sectional HRTEM image with a $10 \times 10 \text{ nm}^2$ field of view, which was taken with a magnification of 800 K, the resolution limit of our microscope

(JEOL ARM200F). From the differences in contrast and the atomic arrangements between the upper and lower parts of this image, we identify the CoSi_2 -Si interface by the dashed line, where the upper part being CoSi_2 , and the lower part being Si. A partial area of $\approx 5 \times 5 \text{ nm}^2$ field size was then cropped from Fig. S2(a) and enlarged in Fig. S2(b), with the boundary line remaining unchanged. The lower part of Fig. S2(b) shows a clear lattice image of the Si(011) plane, and thus allowing us to unambiguously identify the Si atomic positions. Moreover, from the diffraction pattern (DP) of the CoSi_2 part (the DP is shown in the inset of Fig.2(c) in the manuscript), we can clearly identify the orientation of the CoSi_2 lattice and, furthermore, construct a jointed atomic model with the Si lattice. Basing on the Si atomic positions and the boundary line, we map our atomic model on the HRTEM image in Fig. S2(b). The area enclosed by the yellow dashed square was cropped and enlarged again in Fig. S3(a). (This Fig. S3(a) is the same figure shown in the left panel of Fig.5(a) in the manuscript.) Finally, we map the same ball-and-stick model in Fig. S2(b) onto the TEM image of Fig. S3(a) to obtain Fig. S3(b).

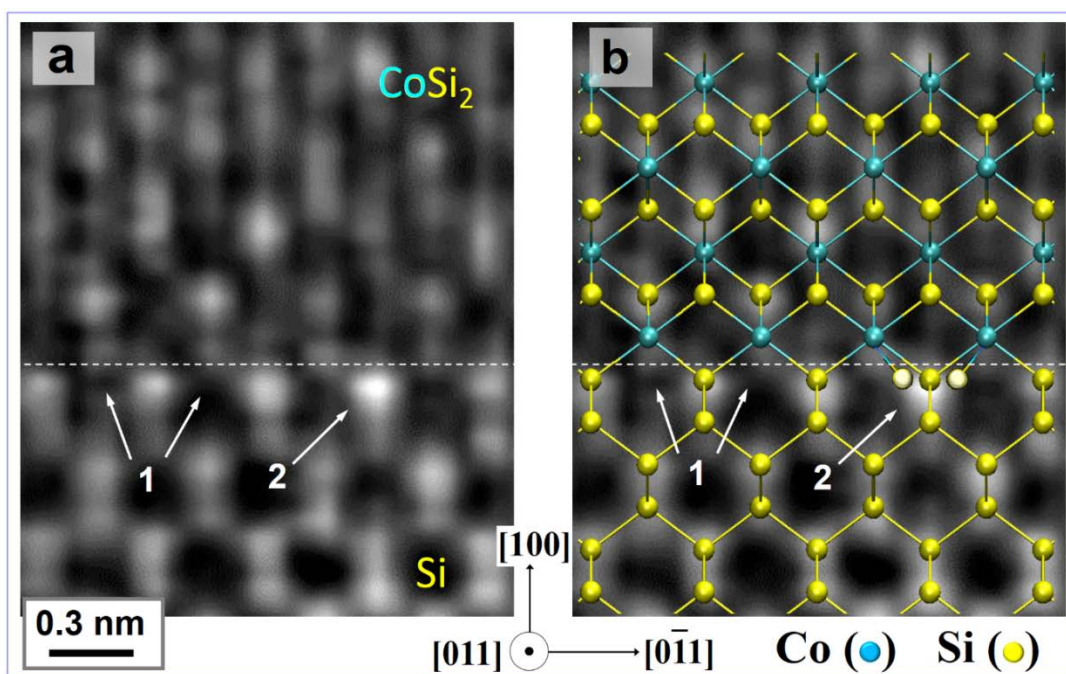


Fig. S3 This figure is the same as the Fig. 5(a) in the manuscript. **(a)** A cross-sectional HRTEM image with epitaxy of $\text{CoSi}_2(100)$ on $\text{Si}(100)$ taken from the yellow dashed box in Fig. S2(b). The field size is $\approx 1.6 \times 2 \text{ nm}^2$. **(b)** A ball-and-stick model projected on the HRTEM image of (a).

In Fig. S3(b), the way for identifying the atomic positions at the interface is the same as above. The resolution for the CoSi_2 image is not ideal, probably owing to the oxidation during the transfer of sample, but it is still satisfactorily acceptable after enlargement for several times. In brief, our

ball-and-stick model does well fit the CoSi_2/Si interface and the Si atomic positions. Hence, the brightest spots nearby the boundary dashed line can be modeled as excess Si atoms, leading to dimer reconstructions at the CoSi_2/Si interface. It should be noted that similar features in the TEM image with a corresponding dimer model explanation was first found and addressed in Ref. [4].

References:

1. Fuchs, K. The conductivity of thin metallic films according to the electron theory of metals. *Mathematical Proceedings of the Cambridge Philosophical Society* **34**, 100-108 (1938).
2. Sondheimer, E. H. The mean free path of electrons in metals. *Advances in Physics* **1**, 1-42 (1952).
3. Hensel, J. C., Tung, R. T., Poate, J. M., Unterwald, F. C. Specular Boundary Scattering and Electrical Transport in Single-Crystal Thin Films of CoSi_2 . *Physical Review Letters* **54**, 1840-1843 (1985).
4. Loretto, D., Gibson, J. M., Yalisove, S. M. Evidence for a dimer reconstruction at a metal-silicon interface. *Physical Review Letters* **63**, 298-301 (1989).